Arabian Journal of Chemistry (2023) **16**, 105020

King Saud University

Arabian Journal of Chemistry

www.ksu.edu.sa
www.sciencedirect.com

ORIGINAL ARTICLE

Schiff-base ligand assisted synthesis of $DyVO_4$/AgBr nanocomposites, characterization, and investigation of photocatalytic activity over organic dye contaminants

Mohammad Hossein Khorasanizadeh [a], Rozita Monsef [a], Masoud Salavati-Niasari [a,*], Hasan Sh. Majdi [b], Waleed Khalid Al-Azzawi [c], Furqan S. Hashim [d]

[a] *Institute of Nano Science and Nano Technology, University of Kashan, Kashan 87317-51167, Iran*
[b] *Department of Chemical Engineering and Petroleum Industries, College of Engineering, Al-Mustaqbal University, Babylon 51001, Iraq*
[c] *Department of Medical Instruments, Engineering Techniques, Al-Farahidi University, Baghdad, Iraq*
[d] *Department of Medical Laboratories Technology, AL-Nisour University College, Baghdad, Iraq*

Received 16 March 2023; accepted 16 May 2023
Available online 22 May 2023

KEYWORDS

$DyVO_4$/AgBr Nanocomposite;
Co-precipitation;
Nanostructures;
UV–Visible Photocatalyst;
Optical degradation

Abstract In the current study, a type-I $DyVO_4$/AgBr heterojunction was prepared by a simple and cost-effective co-precipitation method to obtain a highly efficient photocatalyst for water treatment. The effect of different molar ratios of H_2Salen to dysprosium and temperature reaction was studied on the morphology of the products. As a result of the energy savings, the optimal temperature for the preparation of $DyVO_4$ nanoparticles was chosen as 25 °C, and $DyVO_4$/AgBr nanocomposites were prepared at this temperature. The XRD results revealed that $DyVO_4$ and $DyVO_4$/AgBr nanocomposites were pure in all conditions. A comparative study was conducted between the photocatalytic behavior of $DyVO_4$, AgBr, and $DyVO_4$/AgBr under UV and visible radiation. The photodegradation result reveals that $DyVO_4$/AgBr performs better than pure $DyVO_4$ and AgBr. 79.8% and 72.0% of methylene blue (MB) were degraded by $DyVO_4$/AgBr nanocomposites under UV and visible light after 90 min, respectively. The kinetics study depicts that the higher reaction constant

* Corresponding author.
E-mail address: Salavati@kashanu.ac.ir (M. Salavati-Niasari).
Peer review under responsibility of King Saud University.

Production and hosting by Elsevier

https://doi.org/10.1016/j.arabjc.2023.105020

rate (k = 0.0187 min^{-1}) belongs to $DyVO_4$/AgBr nanocomposite that has the maximum photodegradation.

1. Introduction

Environmental difficulties and energy-related challenges are now two of the main roadblocks preventing the sustainable growth of human society as a result of the industrialization process' ongoing advancement. The ecological environment is under immense stress due to the economies and technologies rapid development, and it is also challenging to supply the enormous demand for energy from human civilization. Considering water contamination, the current rate of industrial waste discharge has a huge negative influence on the environment and residents' health while simultaneously having a substantial adverse impact on the industry's development (Shen et al., 2019). Industrial waste contains a wide range of contaminants. Pharmaceutical and personal care items, organic dyes, and other organic pollutants are all common organic contaminants (Guo et al., 2020; Liu et al., 2018). These compounds pose a serious risk to both the long-term health of the ecosystem and human health since they are very poisonous and difficult to break down using conventional procedures. Organic dye contaminants can have various effects on human health depending on the type and amount of dye present. Some of the potential effects are: i) Skin irritation: Organic dyes can cause skin irritation, itching, and rashes when they come in contact with the skin. ii) Respiratory problems: Inhalation of organic dye particles or fumes can cause respiratory problems such as coughing, wheezing, and shortness of breath. iii) Allergic reactions: Some people may be allergic to certain organic dyes, which can cause severe allergic reactions such as anaphylaxis. iv) Carcinogenicity: Some organic dyes have been found to be carcinogenic or cancer-causing in animal studies. Long-term exposure to these dyes may increase the risk of cancer in humans.v) Neurotoxicity: Certain organic dyes can affect the nervous system and cause symptoms such as headaches, dizziness, and confusion. vi). Reproductive toxicity: Exposure to some organic dyes has been linked to reproductive problems such as infertility and birth defects. Overall, the effects of organic dye contaminants on human health depend on various factors such as the type of dye, exposure level, duration of exposure, and individual susceptibility. It is important to minimize exposure to these contaminants by using safe products and following proper safety measures in industries that use these dyes (Manzoor & Sharma, 2020). The search for low-energy and environmentally acceptable water pollution treatment solutions is currently the subject of global attention. In contrast, the tension carried by ecological problems also advanced environmental technology development. As a result of the ongoing development and invention of technology related to environmental protection, Advanced Oxidation Processes (AOPs), which have high performance and efficiency, have distinguished themselves among environmental governance technologies (Cheng et al., 2016). It is a result of its commonly utilized active species. For instance, most organic contaminants can be effectively degraded by OH. Most biological materials can be mineralized directly to create H_2O, CO_2, and other inorganic materials (Xia et al., 2021). Photocatalysis, among AOPs technologies, is also of tremendous importance in energy conservation since it utilizes clean and plentiful sunlight to accelerate chemical reactions. As a result, photocatalytic technology is a versatile, efficient, and cost-effective water treatment approach (Lan et al., 2021).

Metal oxides, particularly vanadates, are applicable compounds that are gaining popularity in nanotechnology. Their intriguing thermal, biological, electrical, and optical features are developing their usage in multiple industrial fields, including photocatalysts (Guo et al., 2018; Jayaraman et al., 2022; Van Thuan et al., 2022; Abdulhusain et al., 2022; Mahde et al., 2022), catalysts (Palacio et al., 2008), antibacterial agents (Wang et al., 2018), photovoltaic cells (Crespo, 2019), sensors (Ribeiro et al., 2015), and storage cells (Deng et al., 2018). Lanthanide vanadates are the most intriguing vanadate compounds because of their exceptional qualities, which include small bandgap, catalytic, luminescent, and considerable antimicrobial action. Vanadium and lanthanide elements form distinct materials whose qualities are strongly influenced by their crystalline structure, size, content, and surface features (An et al., 2021; Yu et al., 2009). $DyVO_4$, a stable substance with multiple applications, including photocatalyst for degradation of organic dyes, batteries, photoluminescence, and magnetic (Bulbul & Beyaz, 2016; He et al., 2011; Li et al., 2016), is one of the most commonly used types of lanthanide vanadate. Sol-gel, co-precipitation, solvothermal, ultrasonic aided technique, and solid-state are a few chemical approaches described in prior literature to fabricate the nanostructures used in many domains (da Silva et al., 2017; Ghanbari & Salavati-Niasari, 2018; Karami et al., 2020; Wang et al., 2009). Among the reported methods, co-precipitation process highlights a careful control over the kinetic reaction, nucleation, and particle growth with high simplicity, interesting morphologies and regular size distribution (Dong & Koenig, 2020). According to the previous studies, AgBr is a well-known photosensitive semiconductor, which can employ as source materials in photographic films (Li et al., 2013). However, single silver halides show a major shortcoming under light irradiation, due to strong reduction of the interstitial Ag^+ into Ag^0 cluster. Therefore, this response to light results in instability and short lifetime of AgBr in photocatalytic reactions (Ghattavi & Nezamzadeh-Ejhieh, 2020). Since the practical application of AgBr structures in environmental service can be controlled by trapping the photogenerated electron concentration, it is recommended that diverse techniques such as (i) combination them with other semiconductors, and (ii) doping metal or nonmetal elements can effectively modify the lifetime of the charge recombination and subsequently enhance the photocatalytic activity (Cheng et al., 2018; Xie et al., 2023). In this light, the catalysis activities of different coupled semiconductors namely; AgBr/$SmVO_4$ (Li et al., 2013), AgBr/MoO_3 (Feng et al., 2017), AgBr/Bi_2MoO_6 (Jonjana et al., 2016), AgBr/$La_2Ti_2O_7$ (Wang et al., 2019), Ag/AgBr/$GdVO_4$ (Zhang et al., 2018), g-C_3N_4/Ag_3VO_4/AgBr (Barzegar et al., 2018), etc have been explored. However, development of ideal support photocatalyst structures is still needed. This research proposes an approach *via* co-precipitation fabrication of pristine $DyVO_4$ and $DyVO_4$/AgBr nanocomposites and scrutinizes the influence of the molar ratio of precursors to ligand (1:1, 1:2, and 1:0.5) and temperature of reaction on the uniformity and size of the obtained products. The photocatalytic behavior of $DyVO_4$, AgBr, and $DyVO_4$/AgBr nanocomposites was studied over methylene blue (MB) under visible and UV light.

2. Materials and methods

2.1. Materials

Dysprosium (III) nitrate pentahydrate ($Dy(NO_3)_3{\cdot}5H_2O$), Silver nitrate ($AgNO_3$), N,N'- Bis(salicylidene)ethylenediamine (H_2salen), Ammonium metavanadate (NH_4VO_3), and Ammonia (NH_3), were purchased from Merck and applied without further purification. In addition, MB utilized as an organic dye, was obtained from Sigma-Aldrich.

2.2. Synthesis of $DyVO_4$ by co-precipitation

First, 1.44 mmol of H_2Salen, 250 mg of $Dy(NO_3)_3$ (0.72 mmol), and 84 mg NH_4VO_3 (0.72 mmol) were separately dissolved in 25, 30, and 5 mL distilled water, respectively. The solution containing H_2Salen was added to the Dy^{3+} solution. Then, NH_4VO_3 solution was added to the above solution under stirring. Ammonia solution was added dropwise as a precipitating agent (Jovanovic et al., 2018). The resulting precipitate was washed, centrifuged, dried, and calcined at 550 °C for 4 h. Different conditions were tested to achieve the desired sample (Table 1).

2.3. Preparation of $DyVO_4$/AgBr nanocomposites

H_2Salen solution (1.44 mmol) was added to Dy^{3+} solution (0.72 mmol). After 10 min stirring, the solution containing NH_4VO_3 (0.72 mmol) was added to the above solution·NH_3 solution was added drop by drop under stirring. In a separate beaker, AgBr was prepared by adding Ag^+ solution (0.72 mmol, 120 mg) to the Br^- solution (0.72 mmol, 84 mg). The containing AgBr was added to the beaker containing $DyVO_4$, and stirred for 15 min. The precipitate was washed with ethanol several times, and dried at 75 °C (Yu et al., 2018). Finally, the powder was calcined at 550 °C for 4 h.

2.4. Photocatalytic experiment

In a common operation, 30 mg of $DyVO_4$ or $DyVO_4$/AgBr or AgBr were mixed with 30 mL of MB (10 mg/L). Before turning on the lamp, the suspension was then mixed for 30 min in the dark to reach adsorption–desorption balance. Next, a 400 W Osram lamp was turned on, a specific volume of suspension was removed in ate certain intervals. The samples were centrifuged at 9000 rpm for 4 min. In the end, the solution's absorption was checked by UV–Vis spectrophotometry at 665 nm (λ_{max} of MB). The degradation effectiveness (DE) was computed as:

$$DE = \frac{A_0 - A_t}{A_0} \times 100 \quad (1)$$

So that, A_0 and A_t display the initial absorption and final measured absorption at specific time (t), respectively.

3. Results and discussion

3.1. Characterization

Fig. 1a reveals the XRD pattern of pure $DyVO_4$, confirming that all diffraction peaks correspond to $DyVO_4$ (015–0771) with a tetragonal structure. The XRD pattern of pure silver bromide indicates that AgBr with reference code 01–079-0149 (cubic, Fm-3 m) is composed (Fig. 1b). The XRD patterns of $DyVO_4$/AgBr nanocomposites before and after calcination are depicted in Fig. 1(c, d), respectively. As can be seen, the patterns contain $DyVO_4$ and AgBr, with the difference that the intensity of $DyVO_4$ peaks before calcination is very low, which shows that this compound must be calcined.

Table 1 Different preparation conditions for $DyVO_4$.

Sample No.	Molar ratio Dy:V: H_2Salen	Reaction temperature (℃)	Product
1	01:00.5	25	$DyVO_4$
2	01:01:01	25	$DyVO_4$
3	01:01:02	25	$DyVO_4$
4	01:01:02	0	$DyVO_4$
5	01:01:02	50	$DyVO_4$
6	01:01:02	25	$DyVO_4$/AgBr

The FT-IR spectroscopy was employed to characterize the surface modification and structural features of the resultant samples. Fig. 2 (a, b) illustrates the FT-IR spectra of the as-prepared $DyVO_4$ (sample 3) and $DyVO_4$/AgBr nanocomposites in the range from 400 to 4000 cm^{-1}, respectively. As shown in Fig. 2a, the absorption bands in the window of 3200–3600 cm^{-1} can be assigned to the stretching vibrations of OH groups. Also, there is a strong band at around 1630 cm^{-1}, which is due to the bending vibration of adsorbed water. A band at 813 cm^{-1} is due to the coupling vibration between V = O and V – O – V, while the one at 451 cm^{-1} is assigned to V – O – V bending vibration (Karami et al., 2022). However, a weak band around 2924 cm^{-1} is corresponding to the $–CH_2–$ stretching vibrations of ligand on the surface of $DyVO_4$ (Salavati-Niasari & Tavakoli, 2015). For $DyVO_4$/AgBr nanocomposites, the evident interactions between $DyVO_4$ and AgBr show a slow shift on some prominent bands to a lower wavenumber (Fig. 2b).

The effect of different molar ratios of H_2Salen as a ligand was studied on the morphology of $DyVO_4$ nanostructures. Fig. 3(a-f) shows the FE-SEM images of $DyVO_4$ in the presence of different molar ratios of H_2Salen. Fig. 3(a, b) illustrates that the nanoparticles with an average diameter of 36.2 nm (Fig. 5a) are formed as the molar ratio of metal: ligand is 1: 0.5. Some areas show signs of agglomeration. The uniform agglomerated tiny nanoparticles with an average diameter of 26.18 nm (Fig. 5b) are composed when the molar ratio is 1:1 (Fig. 3(c, d)). As can be seen, the homogenous nanoparticles with an average particle size of 52.5 nm (Fig. 5c) are formed using a 1:2 M ratio of metal to ligand (Fig. 3(e, f)). These micrographs reveal that the optimum ratio is 1:2 at room temperature. This molar ratio was chosen for further testing and research into the effect of reaction temperature on particle morphology. The temperature of 0 °C produces strongly agglomerated particles (Fig. 4(a, b) and Fig. 5d). The morphology of $DyVO_4$ prepared at 50 °C (Fig. 4(c, d) and Fig. 5e) is similar to that at 25 °C (Fig. 3(e, f)). As a result of the energy savings, the optimal temperature for the preparation of $DyVO_4$ nanoparticles was chosen as 25 °C, and $DyVO_4$/AgBr nanocomposites were prepared at this temperature. Fig. 4(e, f) depicts the morphology of $DyVO_4$/AgBr nanocomposites with cubic AgBr particles with an average particle size of 175 nm (Fig. 5f) formed next to tiny $DyVO_4$ nanoparticles. Fig. 5(a-f) compares the size distribution diagrams of all samples obtained from Digimizer software, which shows the good distribution of particle size. The TEM images of $DyVO_4$/AgBr nanocomposites are indicated in Fig. 6. As observed, this figure confirms the result obtained from SEM images. The uniform $DyVO_4$ particles with an average diameter of 51 nm in matrix are visible. The elemental analysis (EDS) of pure $DyVO_4$ and binary $DyVO_4$/AgBr nanocomposites displays the high purity of products. The elements, including Dy, V, and O are seen in the EDS spectrum of $DyVO_4$ (Fig. 7a). Also,

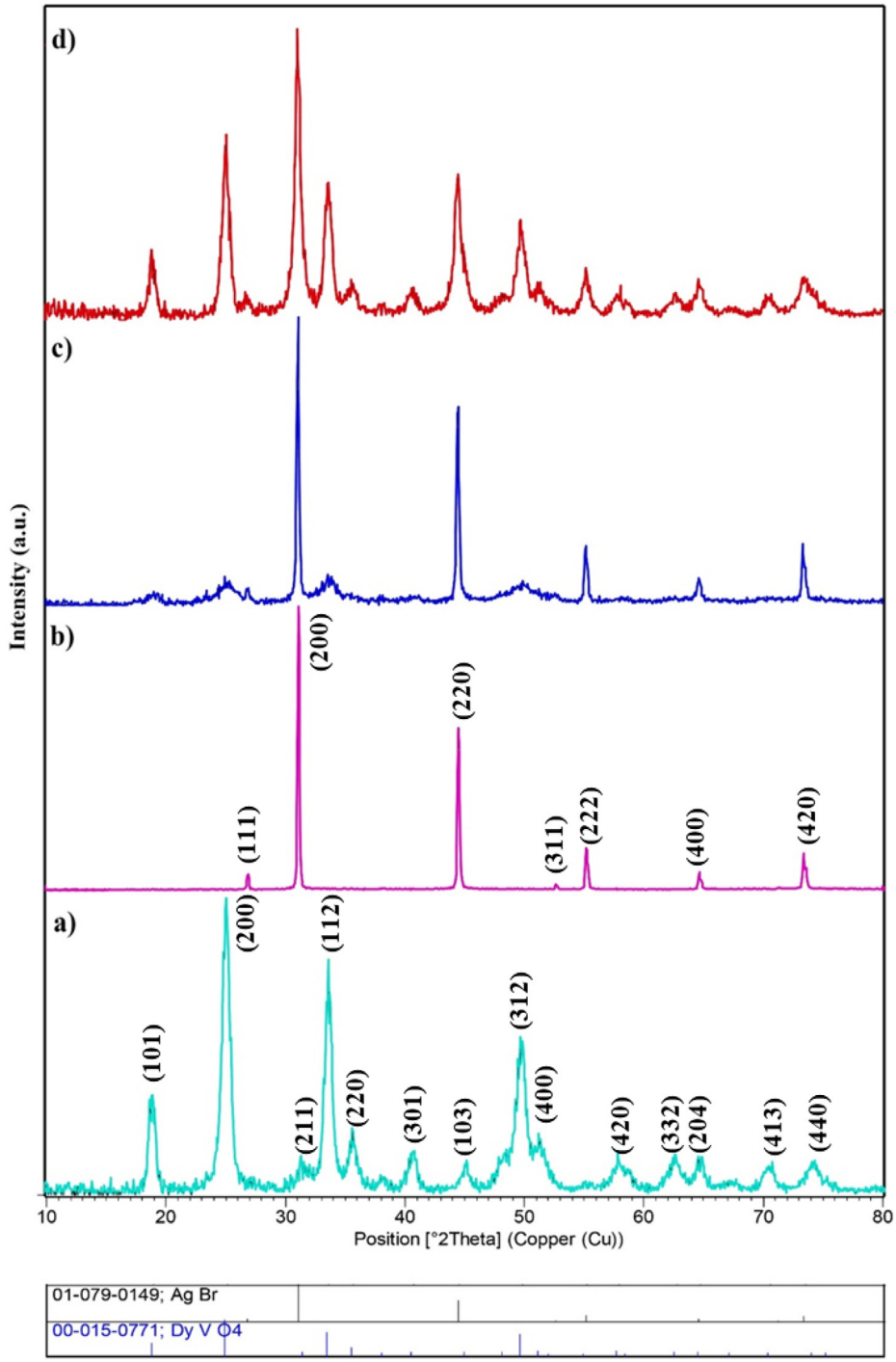

Fig. 1 XRD patterns of (a) $DyVO_4$ (sample 3), (b) AgBr, (c) $DyVO_4$/AgBr nanocomposites before, and (d) after calcination.

in addition to the mentioned elements, Ag and Br are observed in the nanocomposite (Fig. 7b).

The optical bandgap of the oxide compound influences its ability to capture light in photocatalytic reactions significantly. The DRS spectra of $DyVO_4$ and $DyVO_4$/AgBr nanostructures show a number of absorption peaks in the 200–400 nm range (Fig. 8a and 8e). However, for bare AgBr, compare with $DyVO_4$, it can be seen that there is an optical absorption at about 474 nm, which could confirm its performance to absorb visible light (Fig. 8c). The Tauc plots can be used to calculate the bandgap (Tauc et al., 1966). By fitting to a plot of $(\alpha h\nu)^2$ versus hv, $DyVO_4$, AgBr and $DyVO_4$/AgBr depict bandgap energies of 3.19, 2.50 and 3.08 eV, respectively (Fig. 8b, 8d and 8f). When the AgBr nanoparticles were introduced, the photo-excited electron-hole separation and transfer mechanism of $DyVO_4$/AgBr nanocomposites follows an obvious enhancement in photoactivity applications. These compounds can be used as photocatalysts for environmental purposes due to their ability to be quickly activated by light.

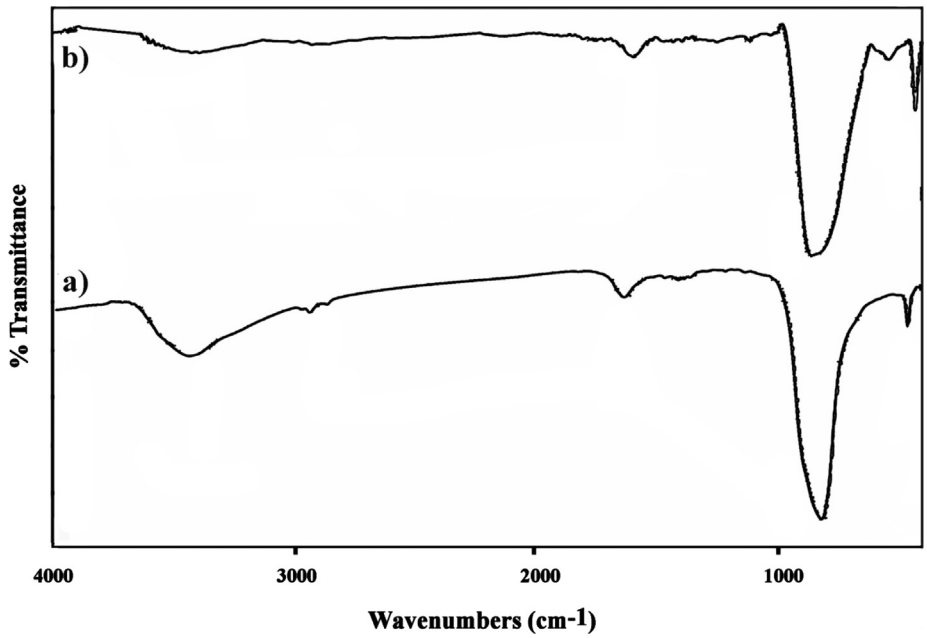

Fig. 2 FT-IR spectra of (a) $DyVO_4$ (sample 3), and (b) $DyVO_4$/AgBr nanocomposites (sample 6).

3.2. Photo sensitive catalytic proficiency& plausible mechanism

MB is a highly colored combination that is employed in textile dyeing and printing and is often found in water pollution. Under UV and visible radiation, $DyVO_4$, AgBr, and $DyVO_4$/AgBr nanocomposites were applied to remove MB from an aqueous solution. Fig. 9a reveals that the degradation percentages of $DyVO_4$, AgBr, and $DyVO_4$/AgBr are 63.0, 74.1, and 79.8%, respectively, under UV light. Besides, under visible radiation (Fig. 9c), the degradation percentages of $DyVO_4$, AgBr, and $DyVO_4$/AgBr are 57.0, 64.7, and 72.0%, respectively.

It is imperative to analyze a complete energy band structure of individual semiconductors in composite for the deep insight of photocatalytic progress over created heterojunction. Therefore, we are intensively interested on the relative band positions of $DyVO_4$ and AgBr components in composite structure. The corresponding conduction band edge (E_{CB}) and valence band edge (E_{VB}) of products can be predicted based on Mulliken electronegativity theory (Jiao et al., 2019). Based on all the observations, a possible type-I heterojunction charge transfer mechanism was suggested upon $DyVO_4$/AgBr nanocomposites for MB degradation. Through calculation, the values of E_{VB} for bare $DyVO_4$ and AgBr nanostructures were evaluated to be 2.88 eV and 2.55 eV vs normal hydrogen electrode (NHE), respectively. Also, the corresponding values of E_{CB} for $DyVO_4$ and AgBr nanostructures were estimated to be −0.30 eV and + 0.05 eV vs NHE, respectively. Specifically, the values of energy levels of the AgBr was enveloped in the relative wide bandgap of $DyVO_4$, which describe the recombination of photo-generated e^- and h^+ according to the type-I $DyVO_4$/AgBr heterojunction (Li et al., 2020). In $DyVO_4$/AgBr heterojunction, a probable mechanism is related to the photo-generated electron-hole separation and facile charge transfer from semiconductor II ($DyVO_4$) to the CB and VB of semiconductor I (AgBr) with a lower band gap. Although charge carriers are agglomerated on the surface of semiconductor I, the difference in recombination rate of charge carriers can act as a key factor on the degradation efficiency.

3.2.1. Hole scavenger scrutiny

The influence of the addition of free radical scavengers in the reaction environment were investigated to survey active trap species. Methanol (CH_3OH), triethanolamine (TEA), disodium ethylenediamine tetraacetic acid ($EDTA^{4-}$), and sodium sulfite (Na_2SO_3), were chosen as hole removers in this study (Fig. 8e). As shown in Fig. 8e, the dye degradation performance when in the presence of TEA decreased slightly (75.3%), while the percentage of dye degradation in the presence of methanol was significant (42.1%). Therefore, the agent considered and active to catalyze dye degradation is hole (h +) (Liu et al., 2019). Methanol (MeOH) is acknowledged to be a more efficient hole scavenger than TEA and bear irreversible and faster oxidation. This can be accomplished by (a) direct interaction of organics with semiconductor valence band (VB) vacancies or trapped holes or (b) reaction of valence band holes with surface hydroxyls by the attack of OH radical group or adsorbed water. These reaction pathways can proceed in parallel and can barely be dignified from each other (Chiarello et al., 2011). In general, the corresponding reactions on the surface of theses catalysts that are responsible for the dye degradation can be illustrated as:

$$Semiconductor\ I + hv \rightarrow e^-(CB\ I) + h^+(VB\ I) \quad (2)$$

$$Semiconductor\ II + hv \rightarrow e^-(CB\ II) + h^+(VB\ II) \quad (3)$$

$$e^-(CB\ II) \rightarrow CB\ I \quad (4)$$

$$e^-(CB\ II) + O_2 \rightarrow \cdot O_2^- \quad (5)$$

$$h^+(VB\ II) \rightarrow h^+(VB\ I) \quad (6)$$

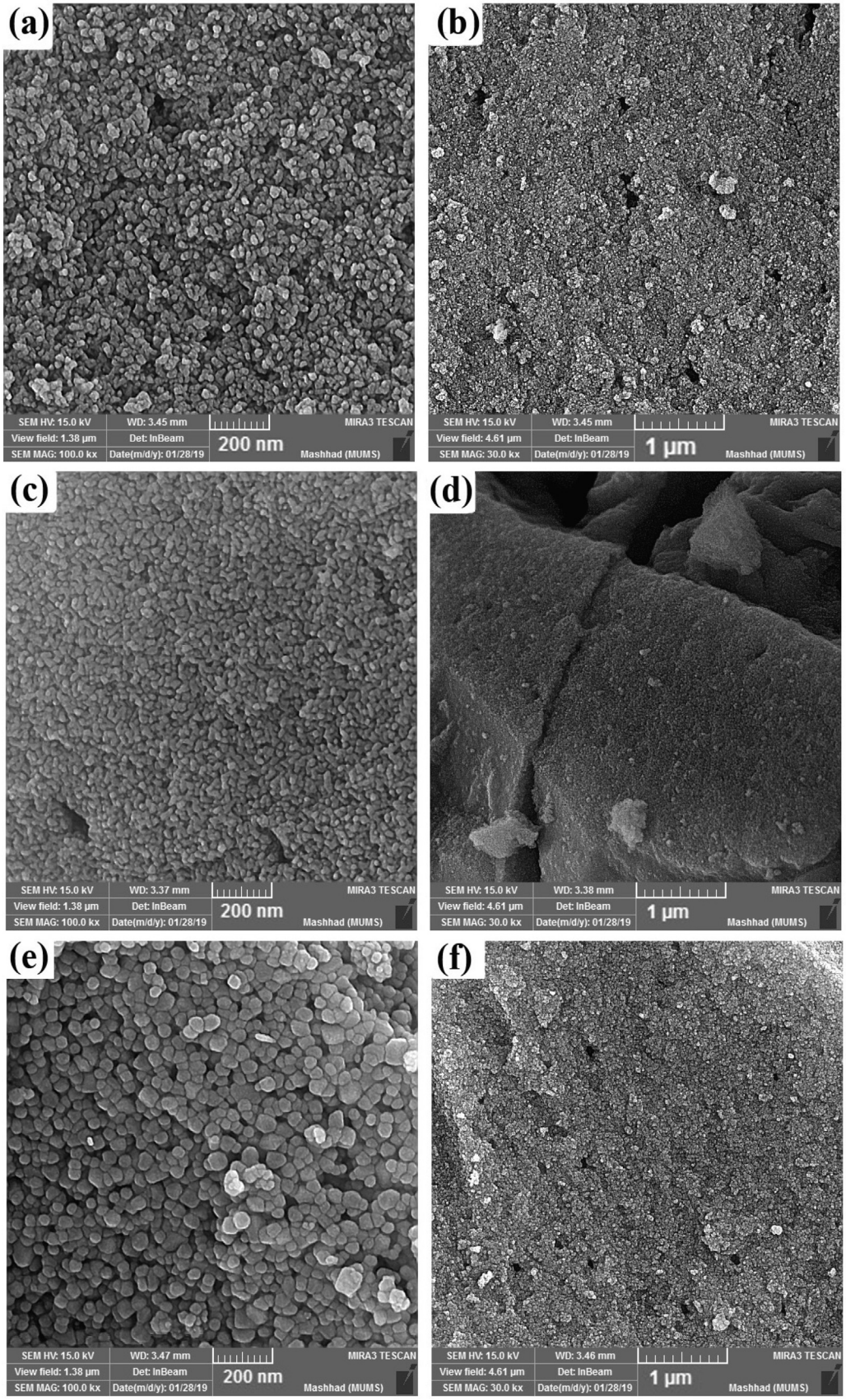

Fig. 3 FE-SEM images of $DyVO_4$ in the presence of different molar ratios of Dy to H_2Salen: (a, b) 1:0.5, (c, d) 1:1, and (e, f) 1:2 at 25℃.

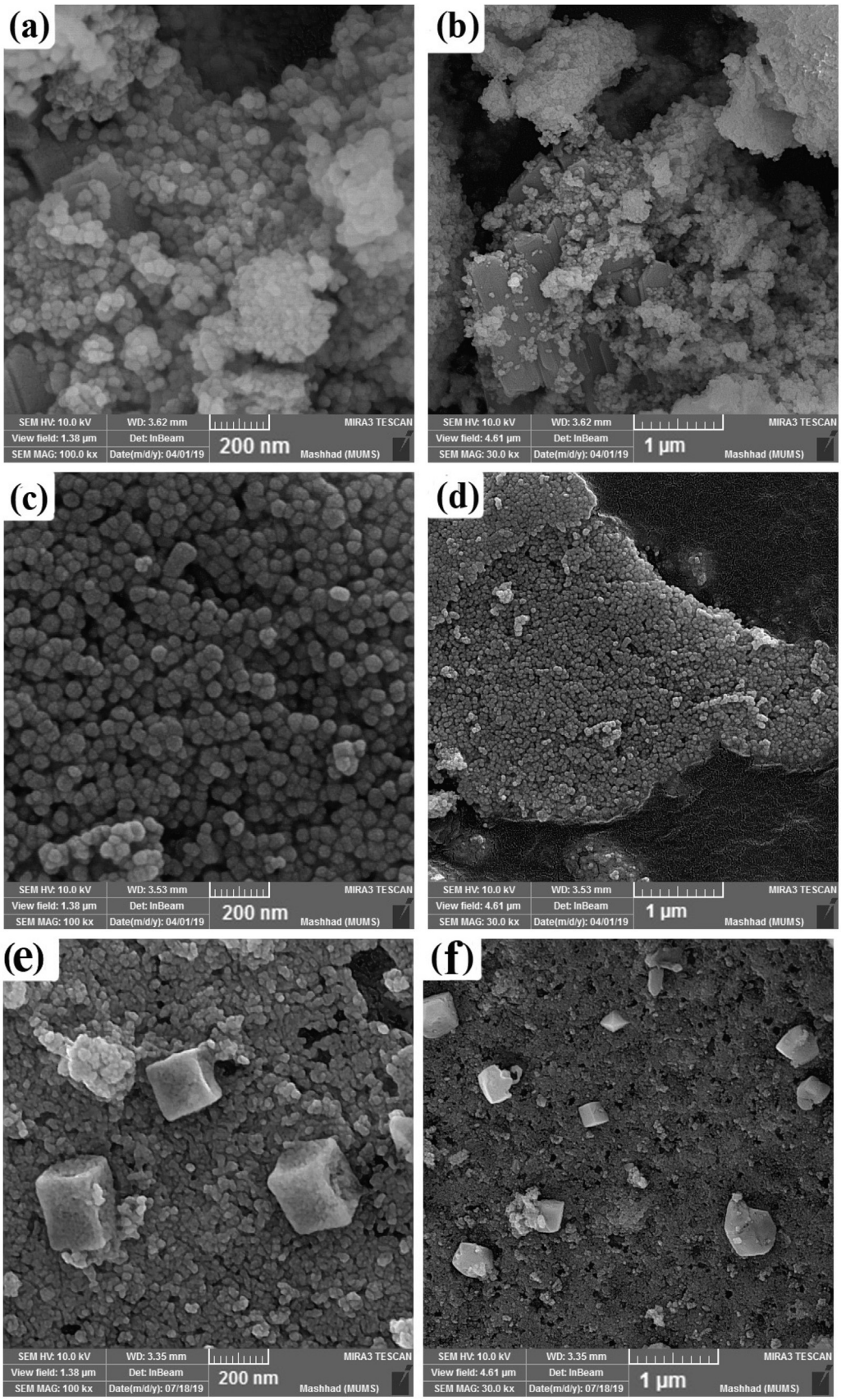

Fig. 4 FE-SEM images of $DyVO_4$ nanostructures in different reaction temperatures: (a, b) 0 °C, (c, d) 50 °C, and (e, f) $DyVO_4$/AgBr nanocomposites prepared at 25 °C.

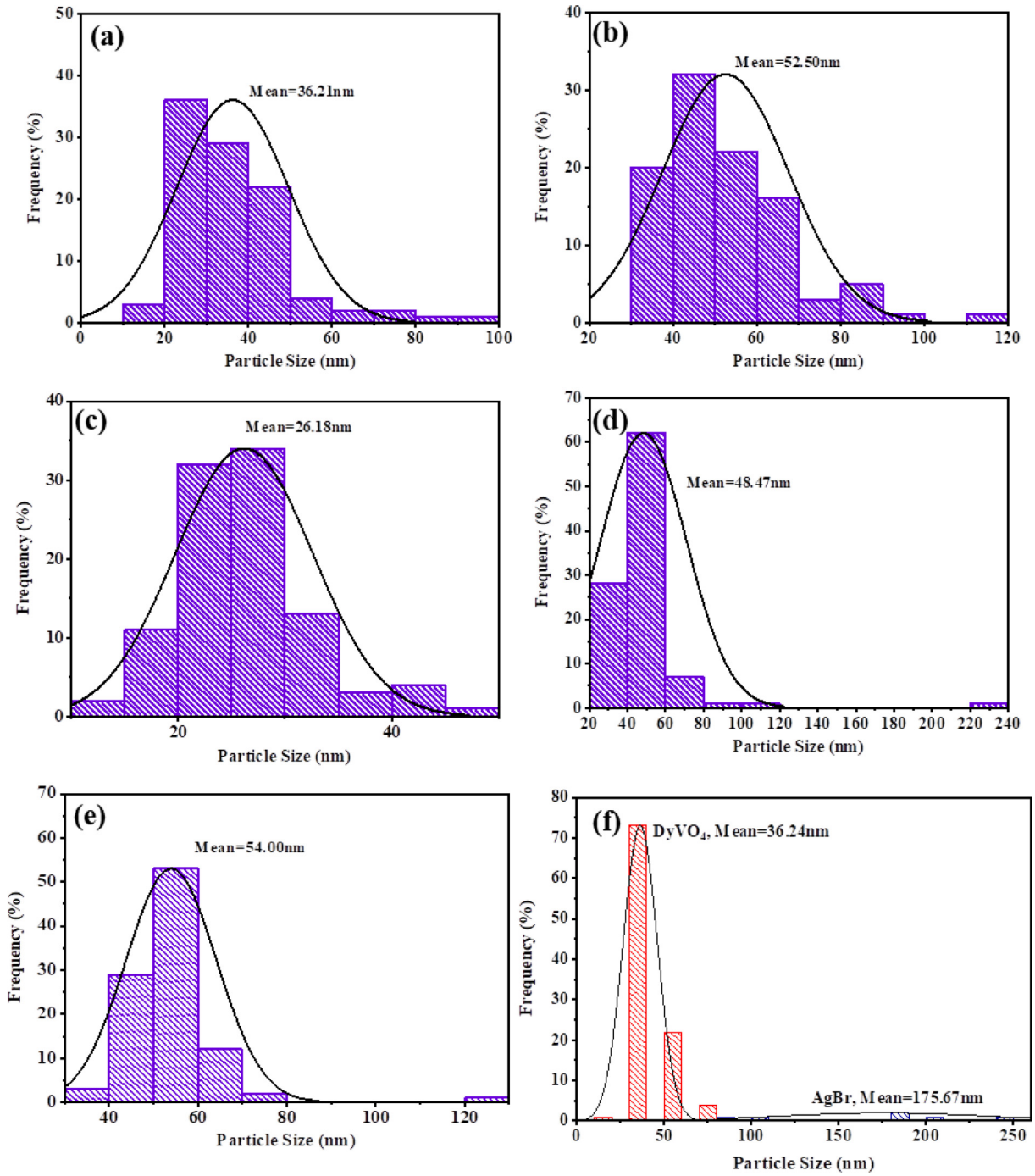

Fig. 5 Size distribution diagrams of $DyVO_4$ nanostructures in the presence of different molar ratios of Dy to H_2Salen: (a) 1:0.5, (b) 1:1, (c) 1:2 at 25℃, in different reaction temperatures: (d) 0 °C, (e) 50 °C, and (f) $DyVO_4$/AgBr nanocomposite at 25 °C.

$$^{\cdot}O_2^- + 2H^+ + e^-(CB\ II) \rightarrow H_2O_2 \quad (7)$$

$$H_2O_2 + e^-(CB\ I) \rightarrow \cdot OH + OH^- \quad (8)$$

$$^{\cdot}O_2^- + H_2O_2 \rightarrow \cdot OH + OH^- + O_2 \quad (9)$$

$$O_2 + 2\,e^-(CB\ I) + 2\,H^+ \rightarrow H_2O_2 \quad (10)$$

$$OH_{free} + h^+(VB\ II) \rightarrow \cdot OH \quad (11)$$

$$OH_{absorbed} + h^+(VB\ I) \rightarrow \cdot OH_{absorbed} \quad (12)$$

$$\cdot OH/\ h^+/\ ^{\cdot}O_2^- + pollutant \rightarrow H_2O + CO_2 \quad (13)$$

Driven by the potential and energy gap difference, it can well explain that the as-prepared nanocomposite follow two interface effect on their photocatalytic system, as irradiation source is changed. It should be noted that the $DyVO_4$/AgBr heterojunction show a high ability of single AgBr structures under visible light due to their small band gap energy. Thus,

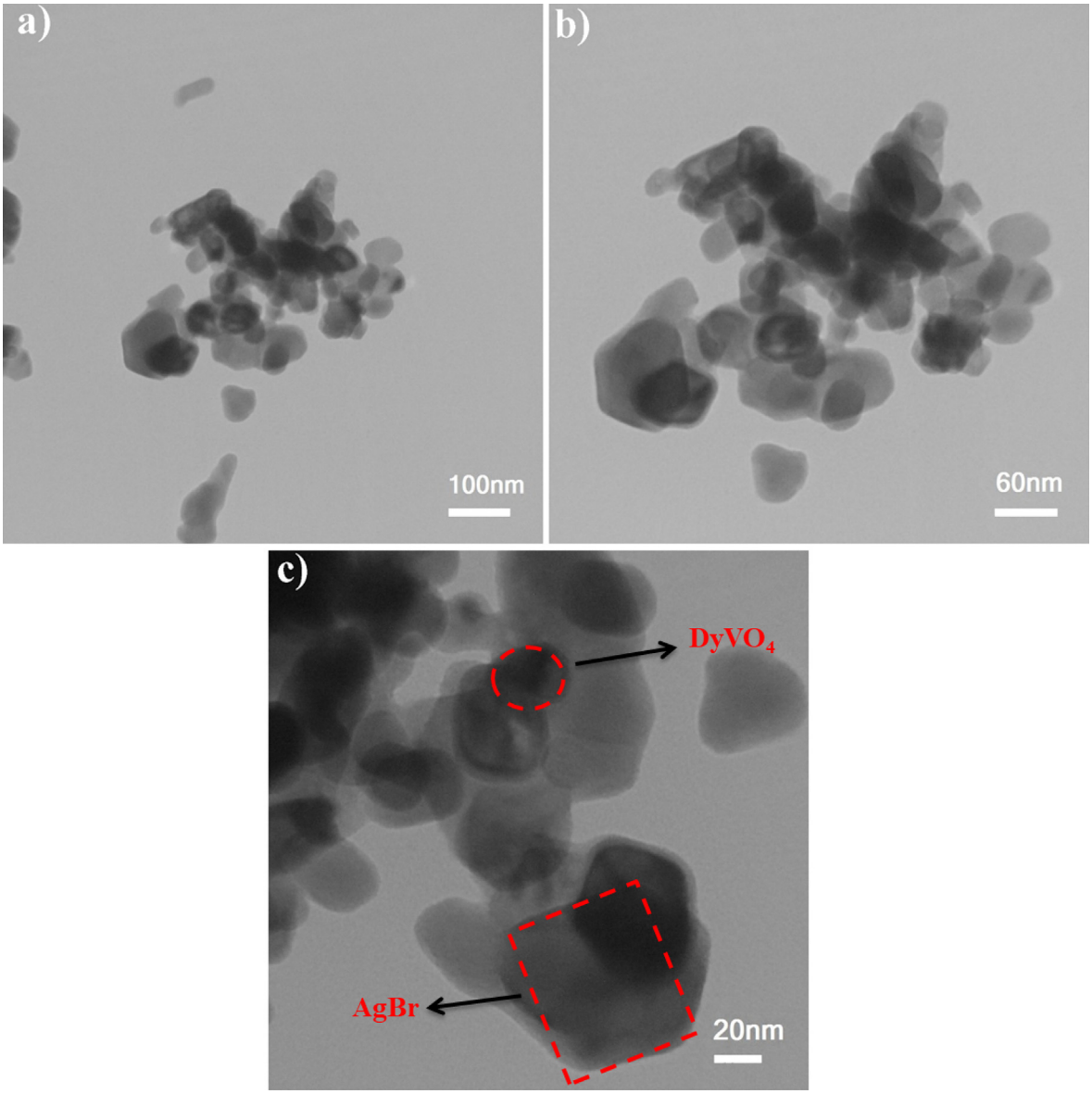

Fig. 6 TEM images of $DyVO_4$/AgBr nanocomposites prepared at 25 °C (sample 6).

this compounds act as a single visible-active photocatalyst during reaction. However, the pristine $DyVO_4$ can be efficiently activated in the presence of UV light irradiation. Based on these results, the photocharges cannot be excited by visible light over the $DyVO_4$ structures, which limit their performance as a Type-I heterojunction photocatalyst under visible light. In this case, the produced photogenerated-electrons on CB and photoinduced-holes on VB in AgBr structures were restricted by visible light. The overall process of photodegradation under visible light can be expressed by the following equations:

$$Semiconductor\ I + hv \rightarrow e^{-}(CB\ I) + h^{+}(VB\ I) \quad (14)$$

$$h^{+}(VB\ I) + H_2O \rightarrow OH^{-} + H^{+} \quad (15)$$

$$OH_{absorbed} + h^{+}(VB\ I) \rightarrow \cdot OH_{absorbed} \quad (16)$$

$$O_2 + 2\ e^{-}(CB\ I) + 2\ H^{+} \rightarrow H_2O_2 \quad (17)$$

$$H_2O_2 + e^{-}(CB\ I) + H^{+} \rightarrow \cdot OH + H_2O \quad (18)$$

$$\cdot OH/\ OH^{-} + pollutant \rightarrow H_2O + CO_2 \quad (19)$$

As a result, under visible light, the possibility of participation of $DyVO_4$ along with AgBr as type-I heterojunctions is eliminated. But, it seems that the interfacial defects in composite texture provide good separation efficiency of charge carriers and thus, the higher photocatalytic activities under visible area. However, under UV light, the type-I heterojunction mechanism for the composite catalyst was established. But, since the standard redox potential of $O_2/^{\bullet}O_2^{-}$ (-0.046 eV vs NHE) is more negative than the CB potential of semiconductor I (+0.054 eV), the accumulated electrons cannot reduce the O_2 species to form $^{\bullet}O_2^{-}$. However, the holes in semiconductor I has the ability to oxidize the H_2O or $OH^{-}$to produce •OH (1.99 eV for OH^{-} /•OH and 2.27 eV for H_2O/•OH), which is corresponding to the relatively more positive VB

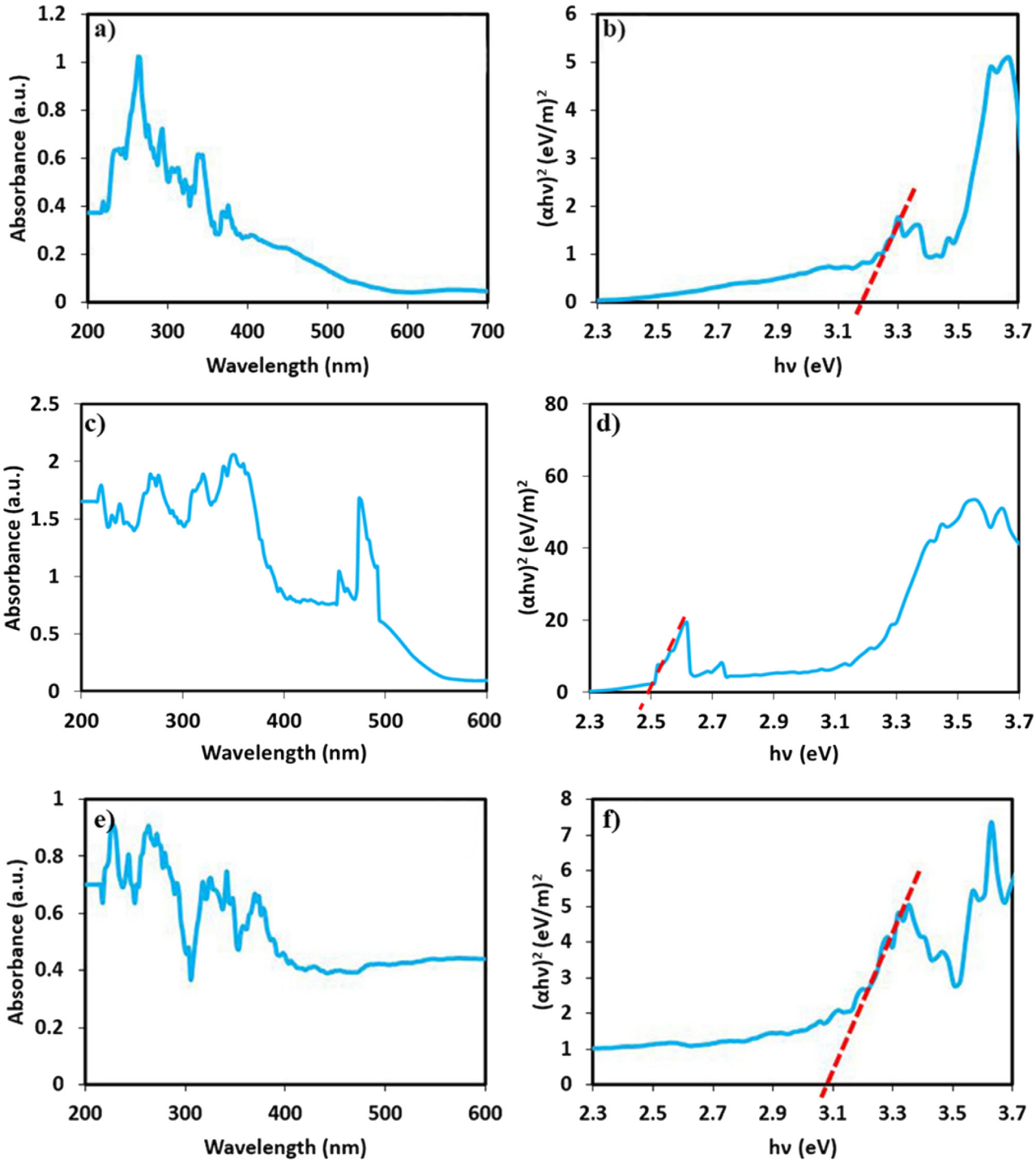

Fig. 8 DRS spectra and Tauc plots of (a and b) $DyVO_4$, (c and d) AgBr, and (e and f) $DyVO_4$/AgBr nanocomposites at 25 °C.

potential (Lu et al., 2019; Wang et al., 2016). By employing type-I heterojunction model, the $DyVO_4$/AgBr nanocomposites could optimize the separation of the electron–hole pair and eventually leading to the high photodegradation efficiency (Scheme 1).

Based on the Langmuir-Hinshelwood mechanism, the possible rate constants of MB were calculated (Yu et al., 2007).

$$\ln\frac{C_0}{C} = kt \tag{20}$$

C_0 and C represent the concentration of organic dyes at first and t time, respectively. The pseudo-first-order rate constant is denoted by k (min^{-1}). Based on linear correlations between reaction time and $\ln(C_0/C)$, the pseudo rate constant (k) has been calculated. The increased photocatalytic efficiency was attained at a higher reaction rate constant, as observed in Fig. 9b and 9d. A comparison of vanadate-based photocata-

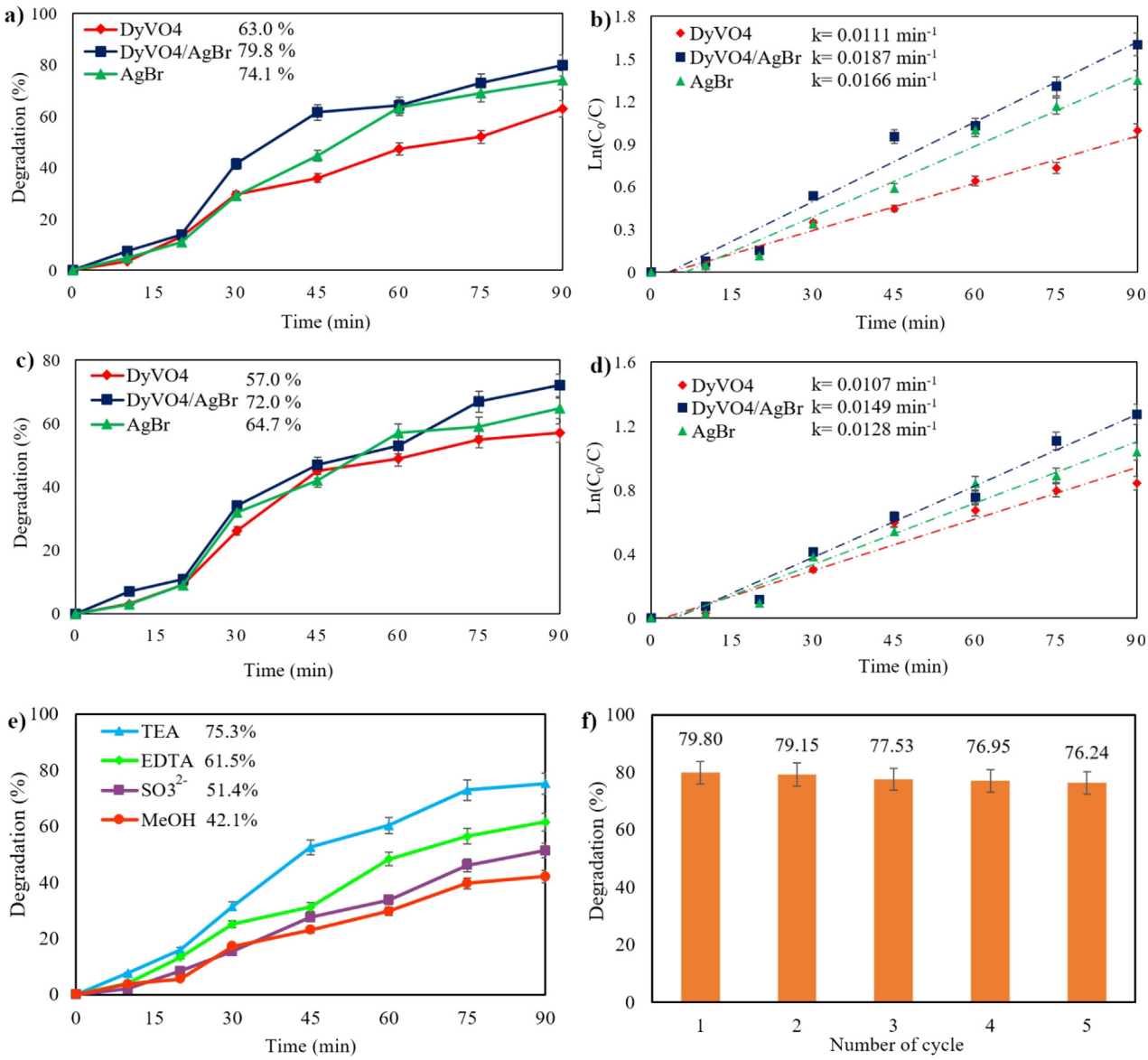

Fig. 9 Photocatalytic degradation and $\ln(C_0/C)$ vs. time of MB over $DyVO_4$, AgBr, and $DyVO_4$/AgBr under (a and b) UV, and (c and d) visible light, e) effect of different hole scavengers, and f) recyclability test.

lysts is given in Table 2. $DyVO_4$, AgBr, and $DyVO_4$/AgBr can sufficiently degrade MB in both UV and visible light sources based on their photocatalytic efficacy.

4. Conclusions

$DyVO_4$ nanoparticles were fabricated by simple co-precipitation method and the effect of different molar ratios of H_2Salen as a ligand to metal (Dy) was investigated. The results indicated that the best molar ratio of ligand to metal was 2:1. DRS spectra showed that the bandgap of $DyVO_4$, AgBr and $DyVO_4$/AgBr was estimated at 3.19, 2.50 and 3.08 eV, making them good candidate for photocatalytic performance. The photocatalytic degradation demonstrated that $DyVO_4$/AgBr nanocomposite has better performance in comparison to every constituent (pristine $DyVO_4$ and pure AgBr) under UV and visible light radiations. $DyVO_4$/AgBr nanocomposite could degrade 79.8% and 72.0% of MB under UV and visible light, respectively. From these results it can be inferred that the increased activity of $DyVO_4$/AgBr nanocomposites can mainly ascribe to type-I heterojunction model under UV light. However, with respect to the charge separation mechanism of composite under visible light, this phenomenon could show the synergy and interfacial defects of two components as the main factors of improved photodegradation rate. The prepared $DyVO_4$/AgBr nanocomposites are of great significance due to its outstanding features, which allow it for use in wastewater treatment.

CRediT authorship contribution statement

Mohammad Hossein Khorasanizadeh: Writing – review & editing, Investigation, Methodology, Formal analysis. **Rozita Monsef:** Formal analysis, Data curation, Writing – review & editing, Investigation, Software. **Masoud Salavati-Niasari:** Software, Formal analysis, Methodology, Writing – review & editing, Writing – original draft, Conceptualization, Supervision, Project administration, Investigation, Data curation,

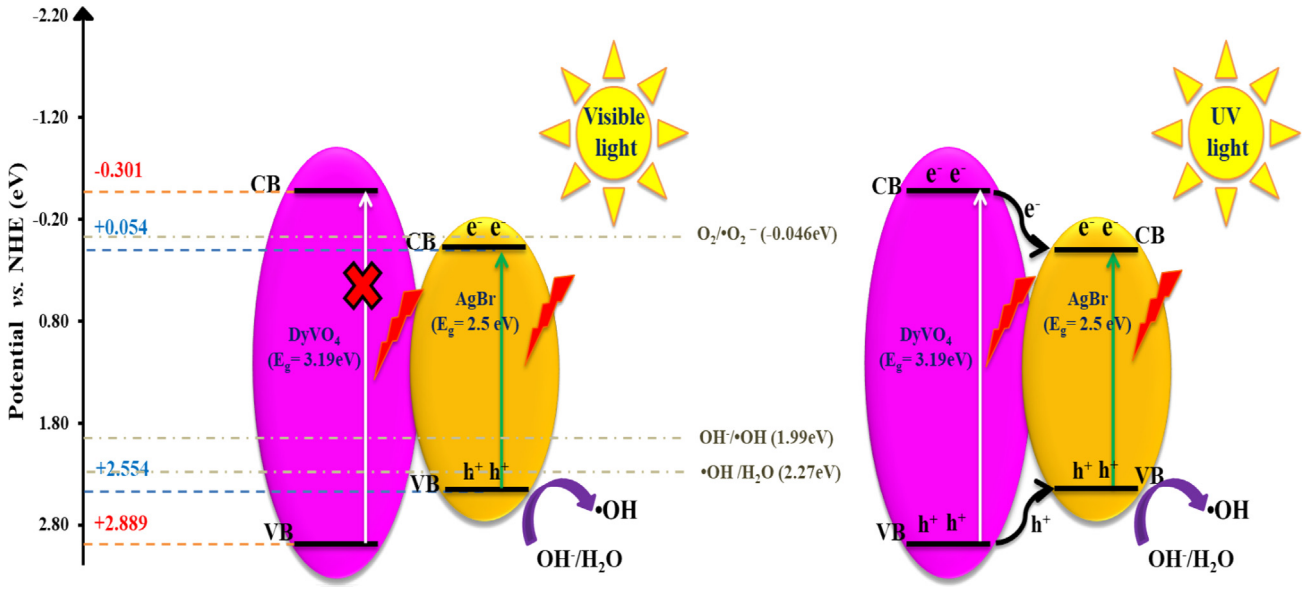

Scheme 1 Schematic diagram of photocatalytic reaction over MB in the presence of $DyVO_4$/AgBr nanocomposites under UV and visible light.

Table 2 Comparison of photocatalytic behavior of different vanadate compounds.

Photocatalyst	Method	Targeted Pollutants	Light Source	Photodegradation time (min)	Degradation (%)	Ref.
$DyVO_4$ AgBr $DyVO_4$/AgBr	Co-precipitation	MB	UV/ Visible	90	63.0/ 57.0 74.1/ 64.7 79.8/ 72.0	This work
$HoVO_4$	Sonochemical	MV[a]	UV	90	67.6	(Khorasanizadeh et al., 2019)
$CeVO_4$/silica fiber	Alcohol -thermal treatment	MB	UV	90	48.5	(Chen et al., 2015)
$NdVO_4$/silica fiber					32.3	(Chen et al., 2015)
$GdVO_4$/silica fiber					64.5	(Chen et al., 2015)
$YbVO_4$	Sonochemical	MB	Visible	120	65.0	(Eghbali-Arani et al., 2018)
$CeVO_4$	Hydrothermal	RhB[c]	UV	80	65.0	(Phuruangrat et al., 2021)
$SmVO_4$	Sol-gel	Carbamazepine	Solar simulator	300	26.6	(Mafa et al., 2021)

[a] Methyl violet, [b] Erythrosine, [c] Rhodamine B.

Validation, Resources, Visualization, Funding acquisition. **Hasan Sh. Majdi:** Writing – review & editing, Software, Data curation. **Waleed Khalid Al-Azzawi:** Writing – review & editing, Software, Data curation. **Furqan S. Hashim:** Software.

Declaration of Competing Interest

The authors declare that they have no known competing financial interests or personal relationships that could have appeared to influence the work reported in this paper.

References

Abdulhusain, Z.H., Mahdi, M.A., Abdulsahib, W.K., Jasim, L.S., 2022. Anabasis articulata exerts an anti-arthritic effect on adjuvant-induced arthritis in rats. J. Adv. Pharm. Technol. Res. 13 (4), 276–280. https://doi.org/10.4103/japtr.japtr_440_22.

An, H.J., Kim, D.H., Ha, H.P., Kim, J., 2021. NO_x reduction consequences of lanthanide-substituted vanadates functionalized with S or P poisons under oxidative environments.

Barzegar, J., Habibi-Yangjeh, A., Akhundi, A., Vadivel, S., 2018. Novel ternary g-C3N4/Ag3VO4/AgBr nanocomposites with excellent visible-light-driven photocatalytic performance for environmental applications. Solid State Sci. 78, 133–143.

Bulbul, B., Beyaz, S., 2016. Strong paramagnetic crystalline LnVO4 (Ln: Gd, Tb, Dy, Ho, Er) nanoparticles synthesized by a fabricating method. Mater. Chem. Phys. 173, 200–204.

Chen, P., Wu, Q., Zhang, L., Yao, W., 2015. Facile immobilization of LnVO4 (Ln = Ce, Nd, Gd) on silica fiber via a combined alcohol-thermal and carbon nanofibers template route. Catal. Commun. 66, 6–9.

Cheng, Q., Deng, X., Zhang, H., Guo, R., Cui, Y., Ma, Q., Zhang, X., Cheng, X., Xie, M., Li, B., 2018. Microwave assisted construction of Ag-AgBr/reduced TiO2 nano-tube arrays photoelectrode and its enhanced visible light photocatalytic performance for degradation of 4-chlorphenol. Sep. Purif. Technol. 193, 255–263.

Cheng, M., Zeng, G., Huang, D., Lai, C., Xu, P., Zhang, C., Liu, Y., 2016. Hydroxyl radicals based advanced oxidation processes (AOPs) for remediation of soils contaminated with organic compounds: a review. Chem. Eng. J. 284, 582–598.

Chiarello, G.L., Ferri, D., Selli, E., 2011. Effect of the CH3OH/H2O ratio on the mechanism of the gas-phase photocatalytic reforming of methanol on noble metal-modified TiO2. J. Catal. 280 (2), 168–177.

Crespo, C.T., 2019. Electronic, magnetic, optical and solar energy absorption properties of the Fe2V4O13 vanadate. Sol. Energy 183, 345–349.

da Silva, G.T., Carvalho, K.T., Lopes, O.F., Ribeiro, C., 2017. g-C3N4/Nb2O5 heterostructures tailored by sonochemical synthesis: Enhanced photocatalytic performance in oxidation of emerging pollutants driven by visible radiation. Appl. Catal. B: Environ. 216, 70–79.

Deng, L., Niu, X., Ma, G., Yang, Z., Zeng, L., Zhu, Y., Guo, L., 2018. Layered potassium vanadate K0. 5V2O5 as a cathode material for nonaqueous potassium ion batteries. Adv. Funct. Mater. 28 (49), 1800670.

Dong, H., Koenig, G.M., 2020. A review on synthesis and engineering of crystal precursors produced via coprecipitation for multicomponent lithium-ion battery cathode materials. CrstEngComm 22 (9), 1514–1530.

Eghbali-Arani, M., Sobhani-Nasab, A., Rahimi-Nasrabadi, M., Ahmadi, F., Pourmasoud, S., 2018. Ultrasound-assisted synthesis of YbVO4 nanostructure and YbVO4/CuWO4 nanocomposites for enhanced photocatalytic degradation of organic dyes under visible light. Ultrason. Sonochem. 43, 120–135.

Feng, B., Wu, Z., Liu, J., Zhu, K., Li, Z., Jin, X., Hou, Y., Xi, Q., Cong, M., Liu, P., 2017. Combination of ultrafast dye-sensitized-assisted electron transfer process and novel Z-scheme system: AgBr nanoparticles interspersed MoO3 nanobelts for enhancing photocatalytic performance of RhB. Appl. Catal. B: Environ. 206, 242–251.

Ghanbari, M., Salavati-Niasari, M., 2018. Tl4CdI6 nanostructures: facile sonochemical synthesis and photocatalytic activity for removal of organic dyes. Inorg. Chem. 57 (18), 11443–11455.

Ghattavi, S., Nezamzadeh-Ejhieh, A., 2020. A visible light driven AgBr/g-C3N4 photocatalyst composite in methyl orange photodegradation: focus on photoluminescence, mole ratio, synthesis method of g-C3N4 and scavengers. Compos. B Eng. 183,. https://doi.org/10.1016/j.compositesb.2019.107712 107712.

Guo, J., Liang, J., Yuan, X., Jiang, L., Zeng, G., Yu, H., Zhang, J., 2018. Efficient visible-light driven photocatalyst, silver (meta) vanadate: synthesis, morphology and modification. Chem. Eng. J. 352, 782–802.

Guo, R., Zeng, D., Xie, Y., Ling, Y., Zhou, D., Jiang, L., Jiao, W., Zhao, J., Li, S., 2020. Carbon nitride quantum dots (CNQDs)/TiO2 nanoparticle heterojunction photocatalysts for enhanced ultraviolet-visible-light-driven bisphenol a degradation and H2 production. Int. J. Hydrogen Energy 45 (43), 22534–22544.

He, H., Zhang, Y., Zhu, W., Zheng, A., Fang, Z., 2011. Controlled synthesis, characterization, mechanism, and photoluminescence property of nanoerythrocyte-like HoVO4 with high uniform size and morphology. J. Cryst. Growth 329 (1), 71–76.

Jayaraman, V., Ayappan, C., Mani, A., 2022. Facile preparation of bismuth vanadate-sheet/carbon nitride rod-like interface photocatalyst for efficient degradation of model organic pollutant under direct sunlight irradiation. Chemosphere 287, 132055.

Jiao, Z., Liu, Z., Ma, Z., 2019. Rodlike AgI/Ag2Mo2O7 heterojunctions with enhanced visible-light-driven photocatalytic activity. ACS Omega 4 (5), 7919–7930.

Jonjana, S., Phuruangrat, A., Thongtem, T., Thongtem, S., 2016. Synthesis, analysis and photocatalysis of AgBr/Bi2MoO6 nanocomposites. Mater. Lett. 172, 11–14.

Jovanovic, D.J., Chiappini, A., Zur, L., Gavrilović, T.V., Tran, L.T. N., Chiasera, A., Lukowiak, A., Dramićanin, M.D., Ferrari, M., 2018. Synthesis, structure and spectroscopic assessment of luminescent GdVO4: Dy3+ and DyVO4 nanoparticles. Fiber Lasers and Glass Photonics: Materials through Applications

Karami, M., Ghanbari, M., Amiri, O., Salavati-Niasari, M., 2020. Enhanced antibacterial activity and photocatalytic degradation of organic dyes under visible light using cesium lead iodide perovskite nanostructures prepared by hydrothermal method. Sep. Purif. Technol. 253, 117526.

Karami, A., Monsef, R., Shihan, M.R., Qassem, L.Y., Falah, M.W., Salavati-Niasari, M., 2022. UV-light-induced photocatalytic response of Pechini sol–gel synthesized erbium vanadate nanostructures toward degradation of colored pollutants. Environ. Technol. Innov. 28, 102947.

Khorasanizadeh, M.H., Monsef, R., Amiri, O., Amiri, M., Salavati-Niasari, M., 2019. Sonochemical-assisted route for synthesis of spherical shaped holmium vanadate nanocatalyst for polluted waste water treatment. Ultrason. Sonochem. 58, 104686.

Lan, J., Wang, Y., Huang, B., Xiao, Z., Wu, P., 2021. Application of polyoxometalates in photocatalytic degradation of organic pollutants. Nanoscale Adv.

Li, T., He, Y., Lin, H., Cai, J., Dong, L., Wang, X., Luo, M., Zhao, L., Yi, X., Weng, W., 2013. Synthesis, characterization and photocatalytic activity of visible-light plasmonic photocatalyst AgBr-SmVO4. Appl. Catal. B: Environ. 138, 95–103.

Li, H., Liu, Y., Cui, Y., Zhang, W., Fu, C., Wang, X., 2016. Facile synthesis and enhanced visible-light photoactivity of DyVO4/g-C3N4I composite semiconductors. Appl. Catal. B: Environ. 183, 426–432.

Li, Y., Wang, X., Huo, H., Li, Z., Shi, J., 2020. A novel binary visible-light-driven photocatalyst type-I CdIn2S4/g-C3N4 heterojunctions coupling with H2O2: synthesis, characterization, photocatalytic activity for Reactive Blue 19 degradation and mechanism analysis. Colloids Surf. A Physicochem. Eng. Asp. 587, 124322.

Liu, M., Luo, L., Dong, F., Wei, H., Nie, X., Zhang, W., Hu, W., Ding, C., Wang, P., 2019. Characteristics and mechanism of uranium photocatalytic removal enhanced by chelating hole scavenger citric acid in a TiO 2 suspension system. J. Radioanal. Nucl. Chem. 319, 147–158.

Liu, Q., Xu, W., Lu, S., Jiang, J., Zhou, J., Shao, Z., Liu, X., Xu, L., Xiong, Y., Zheng, H., 2018. Landscape of emerging and re-emerging infectious diseases in China: impact of ecology, climate, and behavior. Front. Med. 12 (1), 3–22.

Lu, G., Lun, Z., Liang, H., Wang, H., Li, Z., Ma, W., 2019. In situ fabrication of BiVO4-CeVO4 heterojunction for excellent visible light photocatalytic degradation of levofloxacin. J. Alloy. Compd. 772, 122–131.

Mafa, P.J., Malefane, M.E., Idris, A.O., Mamba, B.B., Liu, D., Gui, J., Kuvarega, A.T., 2021. Cobalt oxide/copper bismuth oxide/samarium vanadate (Co3O4/CuBi2O4/SmVO4) dual Z-scheme heterostructured photocatalyst with high charge-transfer efficiency: enhanced carbamazepine degradation under visible light irradiation. J. Colloid Interface Sci. 603, 666–684.

Mahde, B.W., Sultan, A.M., Mahdi, M.A., Jasim, L.S., 2022. Kinetic adsorption and release study of sulfadiazine hydrochloride drug from aqueous solutions on GO/P(AA-AM-MCC) composite. Int. J. Drug Delivery Technol. 12 (4), 1583–1589. https://doi.org/10.25258/ijddt.12.4.17.

Manzoor, J., Sharma, M., 2020. Impact of textile dyes on human health and environment. In: Impact of textile dyes on public health and the environment. IGI Global, pp. 162–169.

Palacio, L., Silva, E., Catalão, R., Silva, J., Hoyos, D., Ribeiro, F., Ribeiro, M., 2008. Performance of supported catalysts based on a

new copper vanadate-type precursor for catalytic oxidation of toluene. J. Hazard. Mater. 153 (1–2), 628–634.

Phuruangrat, A., Thongtem, T., Thongtem, S., 2021. Hydrothermal synthesis and characterization of Dy-doped CeVO4 nanorods used for photodegradation of methylene blue and rhodamine B. J. Rare Earths 39 (10), 1211–1216.

Ribeiro, F.W.P., Moraes, F.C., Pereira, E.C., Marken, F., Mascaro, L. H., 2015. New application for the BiVO4 photoanode: a photoelectroanalytical sensor for nitrite. Electrochem. Commun. 61, 1–4.

Salavati-Niasari, M., Tavakoli, F., 2015. Pb (OH) I-graphene composite: Synthesis and characterization. J. Ind. Eng. Chem. 21, 1208–1213.

Shen, B., Dong, C., Ji, J., Xing, M., Zhang, J., 2019. Efficient Fe (III)/Fe (II) cycling triggered by MoO2 in Fenton reaction for the degradation of dye molecules and the reduction of Cr (VI). Chin. Chem. Lett. 30 (12), 2205–2210.

Tauc, J., Grigorovici, R., Vancu, A., 1966. Optical properties and electronic structure of amorphous germanium. Phys. Status Solidi (b) 15 (2), 627–637.

Van Thuan, D., Nguyen, T.L., Thi, H.H.P., Thanh, N.T., Ghotekar, S., Sharma, A.K., Binh, M.T., Nga, T.T., Pham, T.-D., Cam, D.P., 2022. Development of Indium vanadate and Silver deposited on graphitic carbon nitride ternary heterojunction for advanced photocatalytic degradation of residual antibiotics in aqueous environment. Opt. Mater. 123, 111885.

Wang, F., Zhang, H., Liu, L., Shin, B., Shan, F., 2016. AgV7O18: A new silver vanadate semiconductor with photodegradation ability on dyes under visible-light irradiation. Mater. Lett. 169, 82–85.

Wang, F., Gu, S., Shang, R., Jing, P., Wang, Y., Li, W., 2019. Fabrication of AgBr/La2Ti2O7 hierarchical heterojunctions: boosted interfacial charge transfer and high efficiency visible-light photocatalytic activity. Sep. Purif. Technol. 229, 115798.

Wang, Y., Huang, Y., Ho, W., Zhang, L., Zou, Z., Lee, S., 2009. Biomolecule-controlled hydrothermal synthesis of C-N–S-tridoped TiO2 nanocrystalline photocatalysts for NO removal under simulated solar light irradiation. J. Hazard. Mater. 169 (1–3), 77–87.

Wang, R., Kong, X., Zhang, W., Zhu, W., Huang, L., Wang, J., Zhang, X., Liu, X., Hu, N., Suo, Y., 2018. Mechanism insight into rapid photocatalytic disinfection of Salmonella based on vanadate QDs-interspersed g-C3N4 heterostructures. Appl. Catal. B: Environ. 225, 228–237.

Xia, T., Lin, Y., Li, W., Ju, M., 2021. Photocatalytic degradation of organic pollutants by MOFs based materials: a review. Chin. Chem. Lett. 32 (10), 2975–2984.

Xie, Y., Ding, W., Zhao, J., Luo, J., Lu, R., Shang, T., Xu, Y., Jiang, D., Zhan, Q., 2023. Effects of manganese-doping on the enhanced solar photocatalytic properties of AgBr catalyst: Mechanism and DFT modeling. Appl. Surf. Sci. 607, 154993.

Yu, J., Wang, G., Cheng, B., Zhou, M., 2007. Effects of hydrothermal temperature and time on the photocatalytic activity and microstructures of bimodal mesoporous TiO2 powders. Appl. Catal. B: Environ. 69 (3–4), 171–180.

Yu, C., Yu, M., Li, C., Zhang, C., Yang, P., Lin, J., 2009. Spindle-like lanthanide orthovanadate nanoparticles: facile synthesis by ultrasonic irradiation, characterization, and luminescent properties. Cryst. Growth Des. 9 (2), 783–791.

Yu, C., Xing, P., Wang, C., Zhang, X., Zhao, L., He, Y., 2018. Preparation of AgBr/DyVO 4 composite and its excellent photocatalytic activity in RhB degradation under visible light. Res. Chem. Intermed. 44, 5153–5167.

Zhang, X., Wang, C., Yu, C., Teng, B., He, Y., Zhao, L., Fan, M., 2018. Application of Ag/AgBr/GdVO4 composite photocatalyst in wastewater treatment. J. Environ. Sci. 63, 68–75.